Quantitative observation of geotextile filament structures

Duhwan Kim
Senior Geotechnical Manager, Samsung C&T Coporation, Korea

David Frost
Professor, Georgia Institute of Technology, USA

ABSTRACT: The compression and shear induced micro-mechanical interaction of geotextile filaments and geomembrane surface texture elements have been quantified using needle punched nonwoven geotextiles in combination with smooth/textured HDPE geomembrane. A sample preparation method of epoxy resin impregnation followed by optical image analysis was applied to allow the sensitive geotextile microstructure at different stages of interface shear loading to be observed. The changes in geotextile inner structure were statistically quantified in terms of filament nearest neighbor distance distribution and the variations in filament size distributions were quantitatively evaluated under various boundary conditions. The study provides insight into the mechanism of geotextile microstructure evolution under different boundary conditions.

Keywords: digital image analysis, filament, geotextile, geomembrane, interface shear, nearest neighbor distance distribution, filament size distribution

1 INTRODUCTION

Needle punched nonwoven (NPNW) types are amongst the more common geotextiles used in various field applications. NPNW geotextiles consist of spatially curved filaments that are often assumed to be randomly oriented and/or isotropically distributed. Several approaches to experimentally quantify such fabric structure have been undertaken by researchers. However, each method is known to provide significantly different results for the same nonwoven geotextile (Bhatia and Smith, 1994; Bhatia et al., 1996). Due to difficulties in direct observation, the micromechanical behavior of the internal geotextile structure has received limited attention. In this study, the stress-strain-diameter response of single geotextile filaments is introduced. Then, the effects of compression and interface shearing against geomembranes on the geotextile filament size and microstructure are discussed. The changes in the filament distribution are quantitatively expressed in terms of filament nearest neighbor distance distribution.

2 EXPERIMENTAL PROGRAM AND DIGITAL IMAGE ANALYSIS

2.1 *Materials used*

Materials used in this study include two polypropylene (PP) geotextiles, one polyethylene (PE) geotextile, and a smooth and a textured HDPE geomembranes. The geotextiles are all nonwoven-needle punched and widely used in practice. Detailed information of physical properties about the selected materials are listed in Tables 1 and 2.

Table 1. Physical properties of the geotextiles.

Type	Mass per unit area[1] (g/m²)	Tensile properties[2]		Puncture strength[3] (N)	Trapezoidal tear strength[4] (N)	Apparent opening size[5] (mm)
		σ_y (N)	ε_y (%)			
NPNW-A PP[6]	270	955	50	525	420	0.180
NPNW-B PP	405	1,420	50	835	555	0.150
NPNW-C PE[7]	271	1,023	60	444	356	0.210

*Note*s: [1]ASTM D 5216. [2]ASTM D 4632; [3]ASTM D 4833; [4]ASTM D 4632; [5]ASTM D 4751; [6]Polypropylene; [7]Polyethylene. Data from manufacturers literature.

Table 2. Physical properties of the geomembrane.

Type	Thickness[1] (mm)	Density[2] (g/cm³)	Tensile Properties[3]	
			σ_y (N/mm)[4]	ε_y (%)
HDPE	1.4	0.94	23	13

*Note*s: [1]ASTM D 5199; [2]ASTM D 1505; [3]ASTM D 1603; [4]N/mm-width. σ_y =stress at yield; ε_y=strain at yield. Data from manufacturers literature.

2.2 *Shear response of geotextile-geomembrane interfaces*

The shear failure of geotextile-geomembrane interfaces in the field is known to be accompanied with excessive internal strain of the geotextiles (Mitchell et al., 1990; Seed et al., 1990; Villard et al., 1999). In order to model such a mechanism, a new shear device was developed and used (Figure 1a). A geomembrane specimen, was positioned on a platform mounted on a set of linear bearing rails with the manufacturing machine direction parallel to the shear direction. On top of the geotextile, a footing made of acrylic was lowered. At the bottom of the plate, lubricant was spread and micro film was placed on it to minimize any friction between the footing and the geotextile. The shear frame was held in a plane above the platform base by two rigid shafts installed on either side of the shear platform so that error caused by the contact between the shear box and geomembrane was avoided. (Kim and Frost, 2005; Kim, 2006).
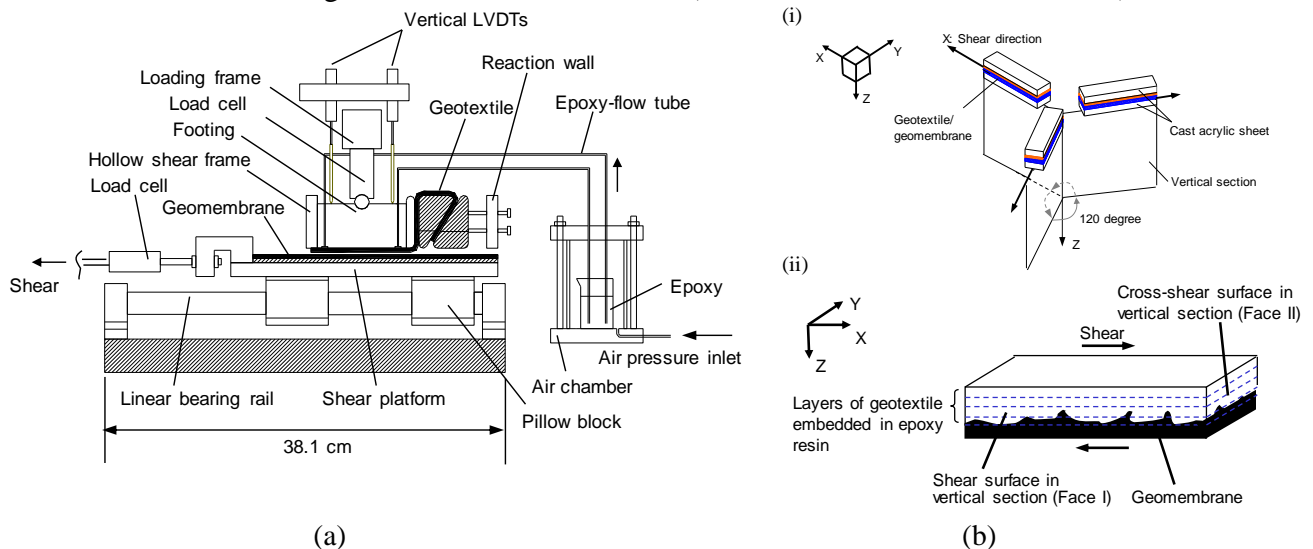

Figure 1. Experimental Setup: (a) Schematic diagram of the interface shear device; (b) dissecting samples for image analysis-(i) tri-sector planes and (ii) three orthogonal viewing planes (Kim and Frost, 2005).
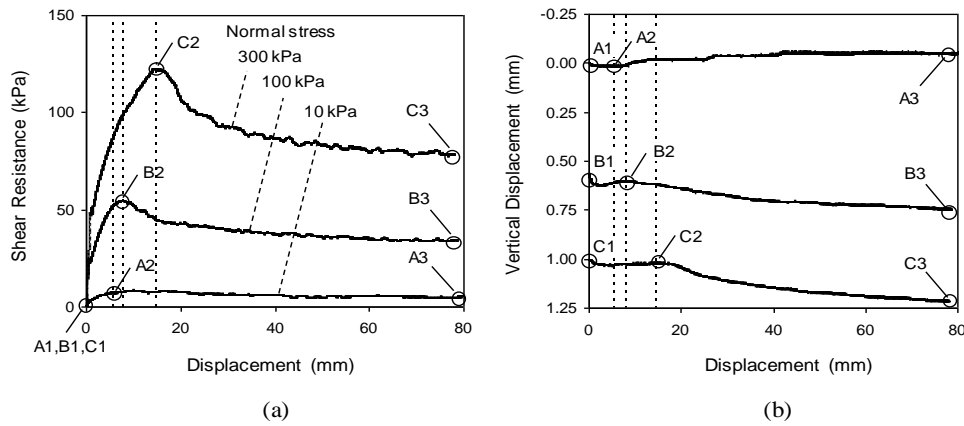
Figure 2. Interface shear response of the geotextile against moderately textured geomembrane: (a) shear resistance; (b) vertical displacement.

Typical results of interface shear resistance of geotextile against moderately textured geomembrane are shown in Figure 2a. It is noted that shear displacement at peak shear resistance increased with normal stress. Figure 2b illustrates the corresponding vertical displacements. After slight compression, the specimen showed dilation under a low normal stress of 10 kPa (A3 in Figure 2b) during shearing while the samples at high normal stresses of 100 kPa and 300 kPa resulted in residual compression after the peaks. Such increasing vertical displacement is due to surface disturbance of geotextiles due to local failure at the interface against the textured geomembrane surface resulting in filament rearrangement.

2.3 *Sample preparation and image analysis technique*

In order to observe the internal microstructure at the geotextile-geomembrane interface, an epoxy impregnation method was adopted to encapsulate the compressed and/or sheared specimen at different boundary conditions. After curing, the specimens were dissected to enable the inner surface to be observed. The trisector method (Gokhale and Drury, 1994) was selected to yield representative coupon surfaces from the specimens that incorporated smooth surfaced geomembranes under various normal stresses (Figure 1b(i)). In contrast, the sheared specimens against textured geomembrane surfaces were cut to expose three orthogonal viewing planes (Figure 1b(ii)). Once polished, images were captured from the various sample surfaces using a high-resolution optical microscope.

3 QUANTITATIVE MICROSTRUCTURE OBSERVATIONS

3.1 *Concept of nearest neighbor distance distribution*

The term nearest neighbor distance is widely used in industrial fields as a descriptor to quantitatively describe spatial arrangement of micro-structural phases in materials. This concept was derived from the Poisson's point process and modified by many researchers. This descriptor is applied on 2-dimensional surface images of materials in conjunction with relevant stereology to minimize biased measurement. The Poisson's theory of distribution can be summarized as follow:

For a random population of points in a space, the probability that at least one point exists in an area dA that surrounds a point is equal to $N_A dA$ where, N_A is the number of features in unit area. The probability that the circumference, dA has exactly q number of points can be expressed in a form as follows:

$$P_r(q) = \frac{(N_A A_0)^q}{q!} \exp(-N_A A_0) \tag{1}$$

The n th nearest neighbor distance distribution can be expressed in terms of a space density function $\psi_n(r)$, which is the probability of finding nearest neighbor in the distance range r to $(r+dr)$.

$$\psi_n(r) = 2\pi r N_A \frac{(\pi r^2 N_A)^{N-1}}{(n-1)!} \exp(-\pi r^2 N_A) \tag{2}$$

For the uniform random distribution of points in space, the nearest neighbors in n th orders are expressed in equation 3 (Stoyan et al. 1987). The numerical values of K_n are shown in Table 3.

$$\langle P_n \rangle = \frac{\Gamma\left(n + \frac{1}{2}\right)}{\sqrt{\pi}(n-1)!} N_A^{-1/2} = K_n N_A^{-1/2} \qquad (3)$$
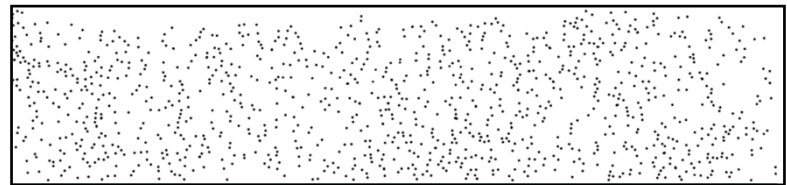
Table 3. Numerical value of K_n (Tewari and Gokhale, 2004).

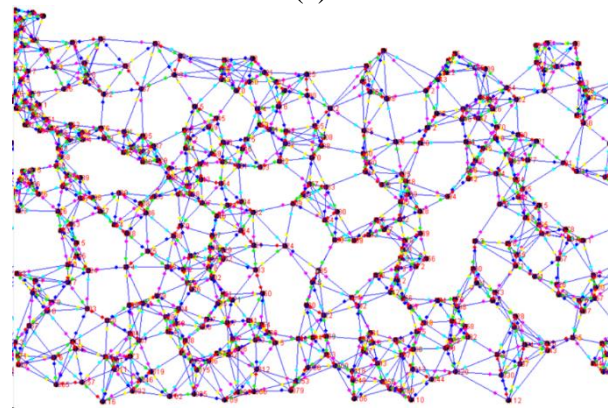| n	1	2	3	4	5	6
K_n	1/2	3/4	15/16	35/32	315/256	693/512

Figure 3 illustrates the process of digital image analysis and measurement of nearest neighbor distances. In this study, a series of distance measurements were conducted with an automated image algorithm programmed in Java.

(a)
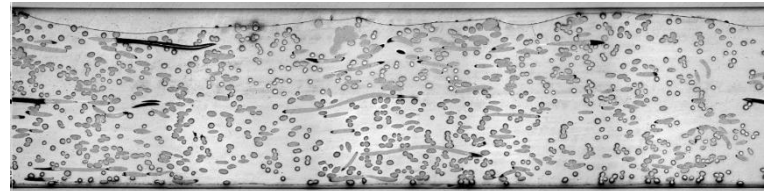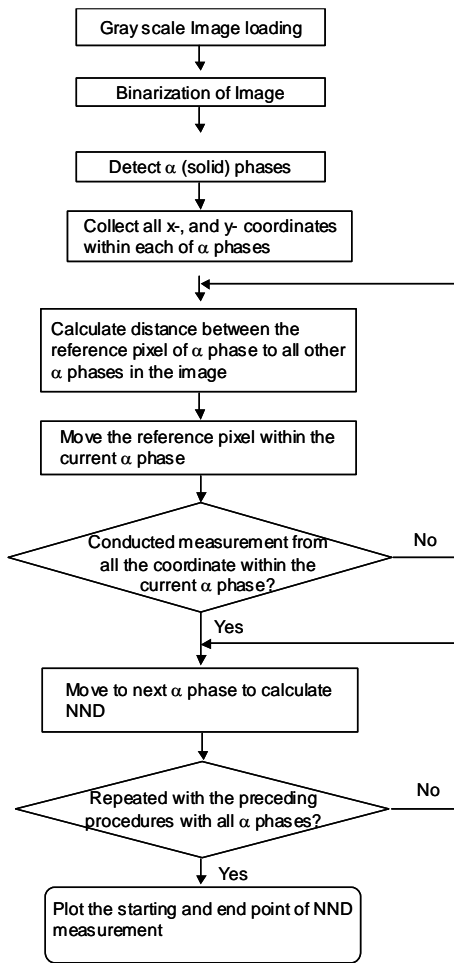
(b)

(c)

(d)

Note: Figure 3c shows first through 5th nearest neighbor features. Only portion of the measurement image is illustrated for clarity.

Figure 3. Process of digital image analysis for NNDD Calculation: (a) Flow chart for program routine; (b) grey scale filament image; (c) detection of center of gravity of each filament phase; (d) resulting NND measurement

The nearest neighbor may be expressed in various definition forms with regard to the shape and density of adjacent features (Kim and Frost, 2007). In this study the distance between center of gravities of the features were measured in order to detect the change of geotextile structure and rearrangement of geotextile filaments.

3.2 *Properties of single geotextile filament*

Tensile properties of single geotextile filaments were measured using an experimental device at the Georgia Institute of Technology for measuring and recording the stress-strain response of filaments. The device had a force resolution of 0.0002 grams, maximum force of $35N$ (3500 gram-force), and strain resolution of $1 \times 10^{-6} \, mm$. The gage length (net measurement length of the filament) is 25 mm, and the extension rate is controlled to a constant value of 0.1 mm/sec. Data are collected at the rate of 10 points per second (100 points per 1 mm extension). All other sample preparation and measurements are conducted based on the procedures described in ASTM D 3379.

Two methods were also tried to measure the filament stress-strain-diameter response. One of the methods additional uses an optical microscope to record the surface image of a single filament while the filament is manually stretched with clamp (Figure 4a). This is a traditional method but still widely used in textile engineering fields. Another method is to use devices using a helium neon gas deflectometer (Figure 4b).
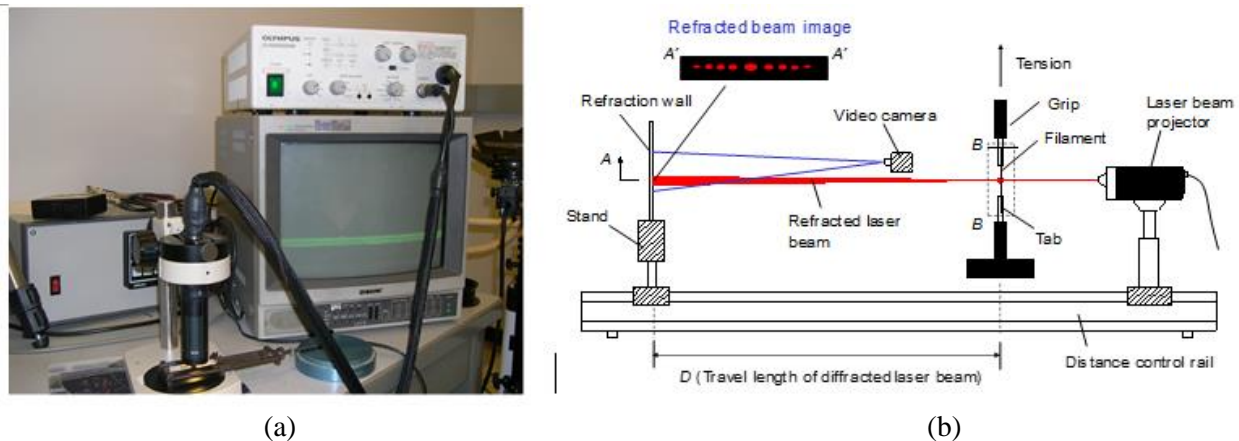

Figure 4. Observation of filament size in axial tension: (a) measurement with optical microscope; (b) use of laser reflectometer.

However, these two methods had limitations in obtaining precise measurement of geotextile filaments. The resolution and clarity of the measurement was limited due to the nature of surface reflection and refraction of the filaments. Thus, results of tensile properties obtained from the two methods were used for comparison purpose and as preliminary study for further image analysis.

The typical tensile behavior of single geotextile filaments is shown in Figure 5. The tensile force versus strain had a nonlinear elasto-perfect plastic form for the two PP geotextiles, resulting in nearly constant resistances after peak until they reached rupture (Figure 5a). The change of filament diameter is also shown as a function of displacement (Figure 5b). The filament from geotextile 'C' made from polyethylene demonstrated a different response. Its initial modulus was relatively high and then decreased at an elongation of about 0.5 mm. This specimen resulted in a constant increase of tensile force until the break point without yielding. Geotextile 'A' was selected for further study using image analysis techniques since it had a relatively large filament size and showed a large and constant rate of change of diameter with tensile strain.
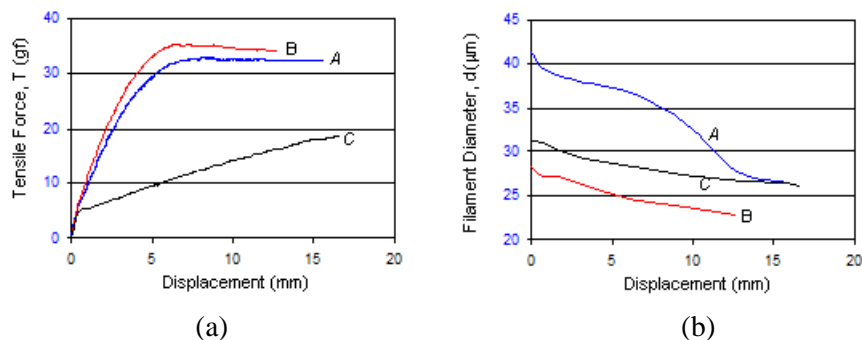

Figure 5. Tensile behavior of single filaments: force-strain-diameter relation: (a) force-displacement; (b) diameter-displacement.

4 RESULTS

4.1 *Nearest neighbor distance distribution*

It is interesting to note that the cumulative frequency distribution for the initial and the unloading states are similar in spite of the apparent irreversible compression of the unloaded specimen (Figure 6). Such results are due to the lateral spreading of the specimen under compression, which resulted in irreversible strain in both vertical and lateral directions and a somewhat larger percentage of larger distances after unloading.

The mean distances of the measured nearest distances in different orders are shown in Figure 7a. The decrease in the coefficient of variation (i.g., ratio of standard deviation to the mean value) of NNDD in Figure 7b indicates the usefulness of higher order NNDD to describe the filament microstructures with less variation.
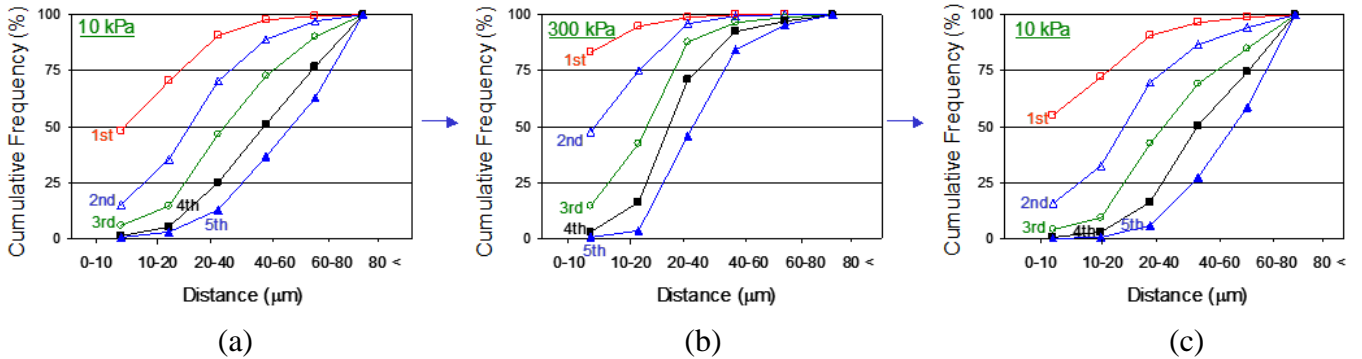
(a)   (b)   (c)

Figure 6. Cumulative NNDD of geotextile filaments: nearest to fifth nearest neighbors: (a) initial at 10 kPa; (b) loading to 300kPa; (c) unloading from 300 to 10 kPa.

Figure 8a shows the variation in the NNDD of geotextile filaments with normal stress in which 56 to 78 % of the filament features have distances smaller than 50 μm to nearest neighbors for tests against smooth geomembrane surfaces. The relatively high value of small distance population for 5th neighbor distances under loading to 300 kPa indicates dense packing of the filaments with low local variation through the specimen section (Figure 8b).
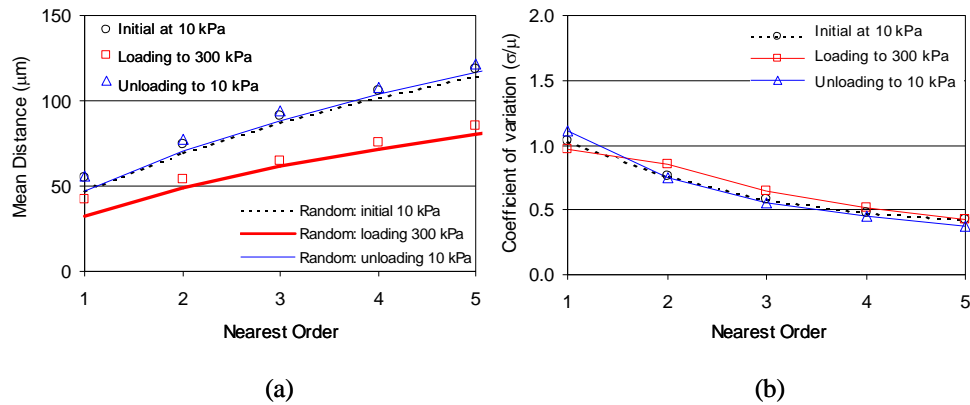

(a)   (b)

Figure 7. Use of Different Order of NNDD: (a) Mean Distances of Randomly Distributed and Actual Filaments with Different Orders; (b) Change of Coefficient of Variation with Orders.
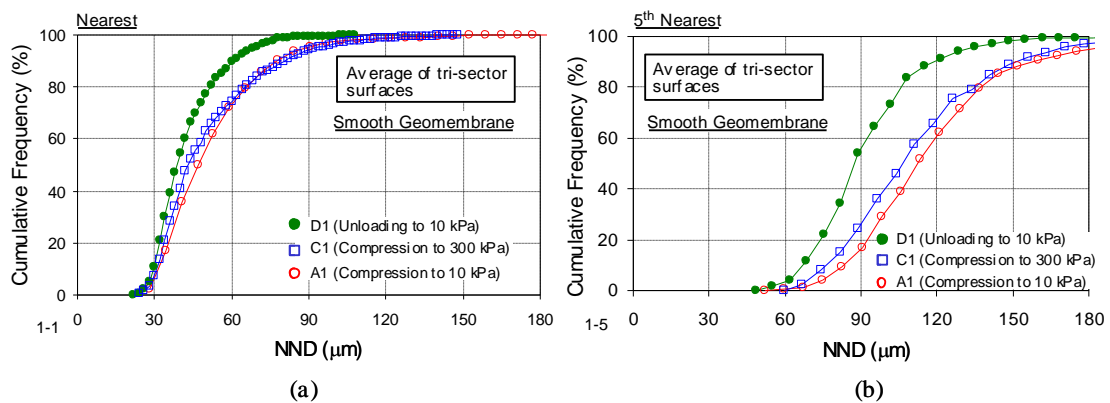

(a)   (b)

Figure 8. Results of NND Measurements from Vertical Sections: Effects of Normal Stress on a Smooth Geomembrane: (a) Nearest; (b) 5th Nearest.

4.2 *Filament size distribution*

Results of the filament size distribution obtained from the vertical sections of the specimens are illustrated in Figures 9 and 10. Figure 9a shows an incremental filament size distribution of a geotextile compressed to 300 kPa on a smooth geomembrane surface. The data is also shown as a cumulative frequency form as well as a model graph of beta distribution which was used to compare the data obtained from different load and boundary conditions. The distribution of initial filament sizes at low normal stress of 10 kPa (A1 in Figure 2) is shown in Figure 10.

(a)   (b)
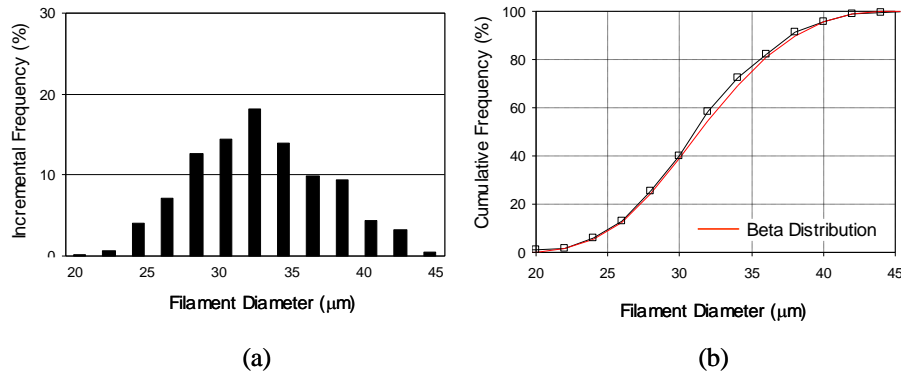
Figure 9. Filament Size Distribution: Compression to 300 kPa; GSE 8-Smooth Geomembrane: (a) Incremental Frequency; (b) Cumulative Frequency.

The change of filament size due to shear against the textured geomembrane is presented in Figure 10a. The data were obtained from the shear surface (face I in Figure 1b) under normal stress of 100 kPa. The filament size corresponding to 50% frequency (D_{50}) decreased by about $6\,\mu m$ at the peak stain. At pseudo residual displacement, the value of D_{50} had recovered by $3\,\mu m$, which is still smaller than at the initial state at normal stress of 100 kPa by about $3\,\mu m$. At both the peak and residual shear states, 90% of filaments remained smaller than $37\,\mu m$. The filaments from specimens under 300 kPa normal stress had slightly smaller diameters compared to the specimens under 100 kPa (Figure 10b). Relatively small changes of filament diameter by about 1.5 μm were found after peak as the specimen was displaced to pseudo residual state of 80 mm. Such a low amount of recovery after peak shear is considered as a result of high contact stress at the interlocking points between the deformed geomembrane textures and by packed filaments.

(a)   (b)

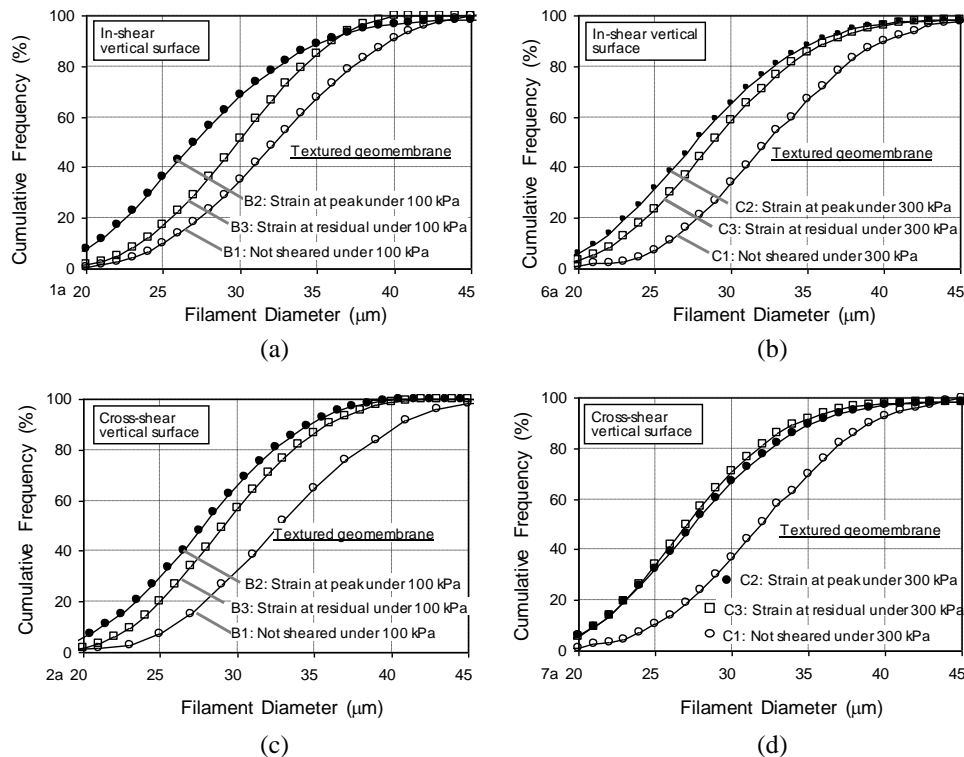(c)   (d)

Figure 10. Results of Filament Size Distribution Measured from Vertical Sections with Various Boundary Conditions: (a) and (b) Effects of Shear on a Textured Geomembrane-Shear Surface (I); (c) and (d) Effects of Shear on a Textured Geomembrane: Cross-Shear Surface (II).

The results from the counter shear surfaces (face II in Figure 1b) which is orthogonal to the shear direction are illustrated in Figures 10c and 10d. A low frequency of filaments smaller than $25\,\mu m$ (F_{25}) was found at peak strain under 100 kPa normal stress compared to the result from the shear surface (face I). A small change was found after peak strain with the D_{50} enlarging to $28\,\mu m$. Similar to the results from the shear surface in Figure 10b, the change of distribution after peak strain was small for specimens at a higher normal stress of 300 kPa (Figure 10d).

Figure 11 shows typical results of filament size distribution: increase of reduced diameters due to elongation of filaments under high normal stress and residual shear state against geomembrane surface textures.
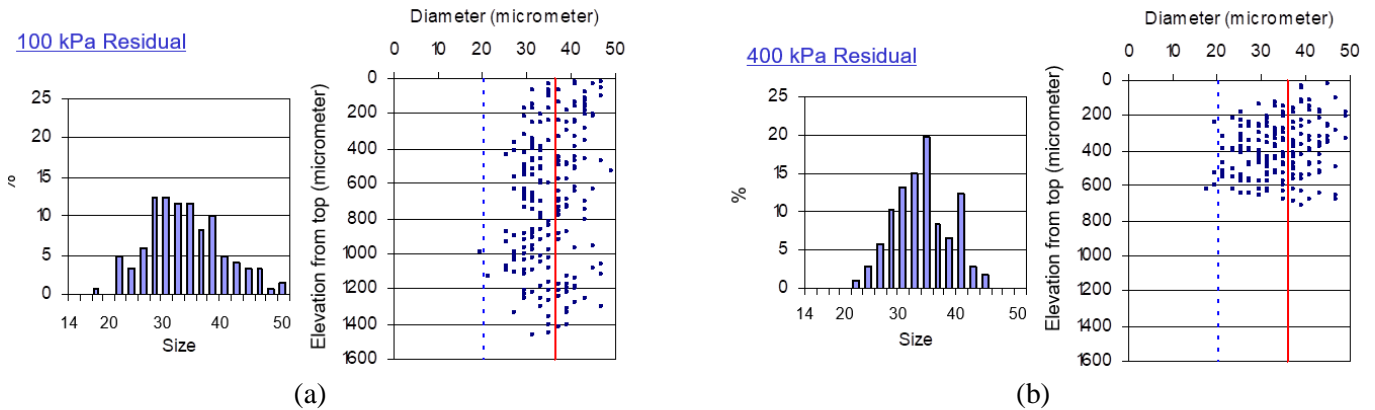
Figure 11. Filament size distribution against moderately textured geomembrane surface - residual shear state: (a) normal stress of 100 kPa; (b) normal stress of 400 kPa.

5 CONCLUSIONS

The tensile properties of filaments in needle-punched nonwoven geotextiles were measured though an experimental program and quantified in terms of the stress-strain-diameter response. Using digital image analysis techniques, the change of filament size and neighboring distance during interface shearing were quantitatively measured and expressed in terms of filament nearest neighbor distance distribution and filament size distribution. The test results showed the impact of the concentrated normal stress and micromechanical interlocking between the geomembrane textures and geotextile filaments during interface shearing. Manufacturers may use this insight to implement processes that can produce filaments that lead to enhanced long-term performance of geotextiles.

REFERENCES

Bhatia, S.K., & Smith, J.L. 1994. Comparative Study of Bubble Point Method and Mercury Intrusion Porosimetry Techniques for Characterizing the Pore-Size Distribution of Geotextiles, Geotextiles and Geomembranes, Vol. 13, pp. 679-702.

Bhatia, S.K., Smith, J.L., & Christopher, B.R. 1996. Geotextile Characterization and Pore Size Distribution: Part III. Comparison of Methods and Application to Design, Geosynthetics International, Vol. 3, No. 3, pp. 301-328.

Kim, D., & Frost, J.D. 2005. Multi-Scale Assessment of Geotextile-Geomembrane Interaction, NAGS 2005/GRI 19 Conference, Las Vegas, 8p.

Kim, D., & Frost, J.D. 2007. Investigation of filament distribution at geotextile/geomembrane interfaces, Journal of Geosynthetics International, Vol. 14, No.3, pp. 128-140.

Mitchell, J. K., Seed, R.B., & Seed, H.B. 1990. Kettleman Hills Waste Landfill Slope Failure. I: Liner System Properties, Journal of Geotechnical Engineering, Vol. 116(4), pp. 647-668.

Seed, R. B., Mitchell, J.K., and Seed, H.B. 1990. Kettleman Hills Waste Landfill Slope Failure. II: Stability Analysis, Journal of Geotechnical Engineering, Vol. 116(4), pp. 669-690.

Stoyan, D., Kendall, W.S., and Mecke, J. 1987. Stochastic geometry and its applications, John Wiley & Sons, 345p.

Dove, J. E., & Frost, J.D. 1996. A Method for Measuring Geomembrane Roughness, Geosynthetics International, Vol. 3, pp. 369-392.

Gokhale, A.M., & Drury, W.J. 1994. Efficient Measurement of Microstructural Surface Area Using Trisector, Metallurgical and Materials Transactions A, Vol. 25A, pp. 919-928.

Villard, P., J. P. Gourc, et al. 1999. Analysis of geosynthetic lining systems undergoing large deformations, Geotextiles and Geomembranes, Vol. 17(1), pp. 17-32.